



Solid-State Dendrite Suppressing Glass-Ceramic Electrolyte for Enabling Lithium Metal Anode

Adrian Grant,^{1,*} Lazbourne Allie,¹ Devon Lyman,¹ Kenechukwu Nwabufoh,¹ Eleston Maxie,¹ Yardlyne Smalley,¹ David Johnson,² and Lonnie Johnson²

¹Johnson Battery Technologies, Atlanta, Georgia 30045, United States of America

²Johnson Research and Development, Atlanta, Georgia, 30045, United States of America

Lithium metal anodes have long been sought to be incorporated into lithium-ion batteries (LiB) in order to increase the energy density and consequently lower the cost of LiB technology. However, Lithium metal is highly reactive and unstable with many known electrolytes. For those electrolytes stable with Lithium, there is also a risk of Lithium dendrite formation during cycling which will lead to an eventual short and catastrophic failure of the battery. In this work, we've developed a patented proprietary ternary glass-ceramic system, $\text{Li}_2\text{CO}_3\text{-Li}_3\text{BO}_3\text{-Li}_2\text{SO}_4$ (Patent number: US10566611B2), via molten synthesis that is stable with Lithium. This can suppress dendrite growth during cycling. The bulk crystalline system exhibits lower conductivity of $2 \times 10^{-6} \text{ s cm}^{-1}$ at room temperature. Using rapid quenching of the system to achieve a semi-crystalline or glass phase improves the conductivity to a modest $2 \times 10^{-5} \text{ s cm}^{-1}$ at room temperature. This method allows ultra-thin deposition of the solid electrolyte to reduce its area specific resistance (ASR) contribution to below $30 \Omega\text{-cm}^2$. Lithium symmetric half-cell cycling of a glass sheet shows stable, dendrite free cycling for at least 350 cycles. These characteristics make this material ideal to use as a solid-state electrolyte (SSE) separator in full cell testing.

© 2021 The Electrochemical Society ("ECS"). Published on behalf of ECS by IOP Publishing Limited. [DOI: [10.1149/1945-7111/abe3a1](https://doi.org/10.1149/1945-7111/abe3a1)]

Manuscript submitted September 1, 2020; revised manuscript received January 15, 2021. Published February 12, 2021.

Lithium-ion batteries (LiBs) revolutionized energy storage and enabled a new age of electronic devices. They are widely used in many electronic devices such as laptops, cell phones, watches, and even vehicles. Since their inception, LiB research has driven the technology closer to its theoretical limits.¹ These limits come with increasing safety concerns including the electrochemical breakdown of the liquid electrolyte at higher voltages and thermal runaway.² Exothermic reactions during cycling can lead to ignition of the flammable organic liquid electrolyte and structural damage of the battery can lead to a short circuit, also with the potential for fire.³⁻⁵ Aside from safety limitations, existing commercial LiBs are currently paired with lower capacity intercalation anodes, such as graphite (372 mAh g^{-1}), rather than utilizing an anode such as lithium metal that has an order of magnitude higher specific capacity (3860 mAh g^{-1}). A lithium metal anode will increase volumetric energy density due to its high specific capacity as well as increasing specific energy due to its lower density (0.53 g cm^{-3}) when compared to graphite.^{6,7} While such improvements can be hard using a lithium metal anode, the main reasons it has not yet been commercialized are: instability of pure lithium metal with organic liquid electrolytes, causing parasitic reactions that results in a high impedance interface and low coulombic efficiency.⁷ And most importantly, safety issues associated with lithium metal anode forming dendrites during cycling, leading to unpredictable short circuits. This can result in thermal runaway and in the presence of a highly flammable organic liquid electrolyte can create a safety hazard.⁸ Progress has been made to try and overcome these issues, by using a buffer layer to reduce interface impedance between liquid electrolyte and lithium metal⁹⁻¹² and use of solid state electrolytes in an effort to slow dendrite growth.^{13,14}

All-solid-state batteries (SSBs) have become central for research into battery advancement for quite some time now because of their potential of higher energy density.¹⁵ The use of a solid in place of a flammable organic liquid electrolyte makes them inherently safer than their existing liquid LiB counterparts. SSB's also offer advantages because of their stability, long cycle life and can also operate across a wide range of temperatures without fear of ignition or freezing of the solid electrolyte making them more versatile than existing battery designs. While some SSE's such as garnet or LiSICON electrolytes for example $\text{Li}_7\text{La}_3\text{Zr}_2\text{O}_{12}$ (LLZO) and

$\text{Li}_{10}\text{GeP}_2\text{S}_{12}$ (LGPS) have similar or higher ionic conductivity compared to organic liquid electrolytes,¹⁶ SSE's still have major challenges to overcome. Of main concern is the electrochemical stability of these higher conducting solids with lithium metal anode^{11,12,17,18} as well as the formation of dendrites through the SSE. We have seen based on literature that dendrites form in SSE's such as the crystalline structure of LLZO^{19,20} and polymer electrolyte such as poly(ethylene oxide) (PEO).²¹

To achieve favorable energy and power densities of the battery, the solid electrolyte separator layer must be extremely thin in order to reduce its contribution to the overall impedance, weight and volume of the battery.²² One candidate in literature that satisfies all the above mentioned conditions is Lithium phosphorus oxy-nitride (LiPON), developed by Dr John Bates et al.²³ in the early 1990s at Oak Ridge National Laboratory. LiPON was found to be stable with lithium metal, has been shown to prevent dendrites^{15,24,25} and is able to be applied sufficiently thin ($< 1 \mu\text{m}$) which is necessary because of its lower conductivity of $\sim(1-3) \times 10^{-6} \text{ s cm}^{-1}$ at room temperature.^{6,10,23,26} The primary drawbacks for LiPON are its expensive application method and low conductivity. LiPON is deposited using RF magnetron sputtering under high vacuum which makes it extremely expensive to scale to commercial production levels.^{15,27}

In order to overcome the issues plaguing SSBs, we focused on oxide based electrolytes that could be developed using economically scalable processes. An ideal electrolyte separator would be stable with Lithium metal, prevent Lithium dendrites, able to be applied using commercially viable processes as a thin film, composed of low cost components, and is possible to be integrated into a hybrid solid-liquid as well as an all-solid-state battery. While the ultimate goal is to make an energy and power dense all-solid-state battery, there is an intermediate solution to be had in the form of a hybrid solid-liquid battery by integrating a solid electrolyte into the current commercial organic liquid electrolyte battery,^{28,29} thus enabling the use of lithium metal anode and increasing the gravimetric and volumetric energy density of the battery. In this paper, we report the preparation and electrochemical properties of a patented³⁰ proprietary oxide based ternary glass-ceramic system $\text{Li}_2\text{CO}_3\text{-Li}_3\text{BO}_3\text{-Li}_2\text{SO}_4$ that can be formed using low cost melt-quenching apparatus and subsequently applied to metal substrates or solid-state cathodes as a thin film of sufficient thickness to reduce the footprint of the separator in the battery. This glass could either be applied in a solid-liquid hybrid or all-solid-state battery. Electrochemical properties and symmetric lithium half-cell cycling were evaluated using AC

*Electrochemical Society Member.

^zE-mail: agrant@johnsonbatterytech.com

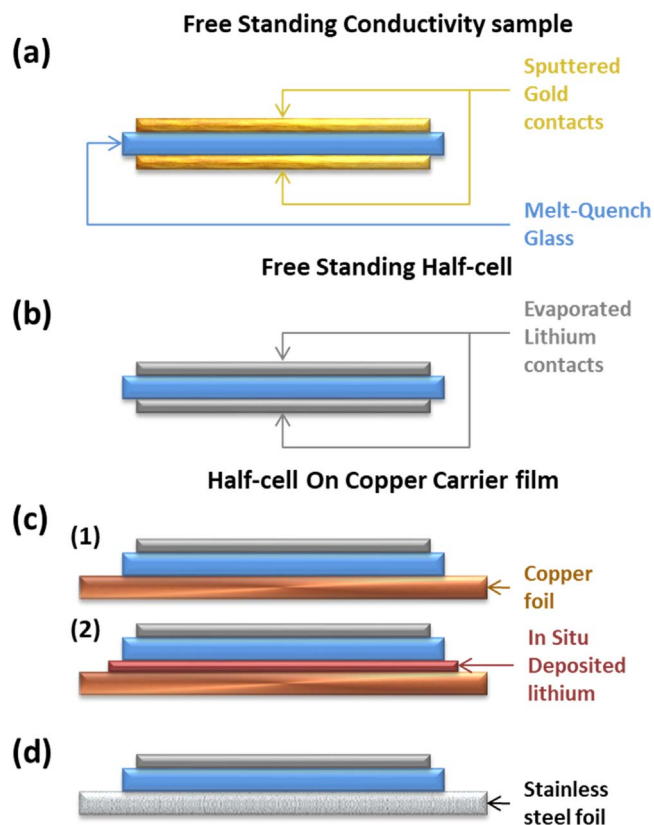


Figure 1. Types of samples used for electrochemical characterization of glass-ceramic electrolyte (colored layers are consistent throughout the different layouts).

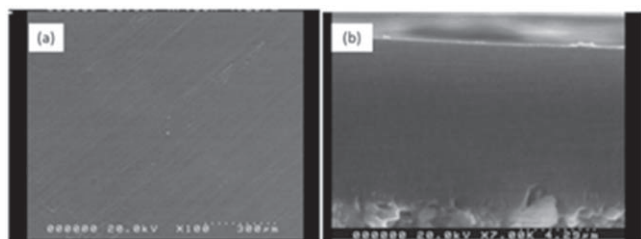


Figure 2. SEM images of the surface (a) and cross section (b) of the glass.

impedance measurements and galvanostatic cycling tests respectively. Structural analysis was performed using SEM and XRD.

Experimental

Starting materials were Li_2O_2 (95%; Sigma Aldrich Chemical Company), $\text{Li}_2\text{B}_4\text{O}_7$ (99%; Thermo Scientific), Li_2CO_3 anhydrous (99%, Thermo Scientific), and Li_2SO_4 anhydrous (99.7%; Thermo Scientific). A mixture of Li_2O_2 and $\text{Li}_2\text{B}_4\text{O}_7$ was milled using yttria-stabilized zirconia milling balls in a milling jar at 400 rpm for 8–15 h. Thereafter, the milled powder was heated in O_2 at 80 °C for 2 h, followed by 120 °C for 3 h, and finally 600 °C for 6 h using a ramp rate of 10 °C min^{-1} to obtain crystalline Li_3BO_3 . The glass-ceramic system was prepared by molten synthesis using a melt quenching technique. A mixture of Li_2CO_3 , Li_3BO_3 , and Li_2SO_4 , was heated in an Al_2O_3 crucible at 800 °C for 0.5–1 h in air until a homogenous melt was achieved. The melt was then poured and quenched with stainless steel quenching plates to form semi-crystalline sheets.

Electrochemical impedance spectroscopy (EIS) measurements and XRD analysis were conducted on a few sheets ranging from

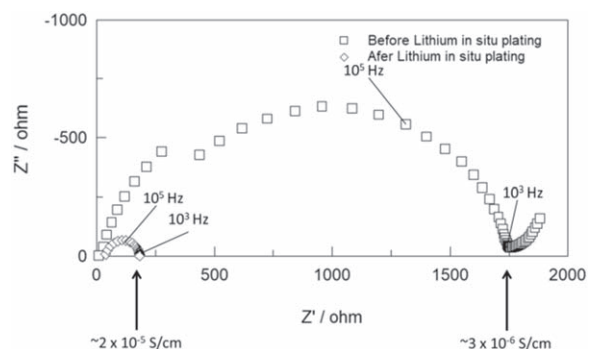


Figure 3. Nyquist plot of melt quench glass of 10 μm thickness and 0.2 cm^2 area on copper foil at room temperature as seen in Fig. 1c before (open square) and after (open diamond) in situ lithium deposition at room temperature.

5–25 μm thick and areas between 0.08–1 cm^2 to confirm ionic conductivity and crystal structure. Gold blocking electrodes were deposited on both sides of the sheets via RF vacuum sputtering for conductivity measurements. AC impedance measurements were conducted using a SI-1260 Solartron impedance analyzer. The frequency range and applied voltage used were 32 MHz to 1 Hz and 10 mV respectively. The remaining sheets were mechanically milled in an Across International PQ N2 planetary ball mill with zirconia balls to reduce to fine powder for melt quenching. The milled powder was melted in an inert Argon environment at 600 °C and thin glass-ceramic sheets were made using a make-shift twin roller quench apparatus. XPS (Kratos Analytical Axis Nova) and XRD (SCINTAG INC XGEN—4000) measurements were conducted on the sheets to determine the chemical composition and crystalline state of the material. Four types of glass-ceramic samples as shown in Fig. 1 were made using the melt quenched apparatus. The first layout as shown in Fig. 1a had Au blocking electrodes sputtered on both sides of the glass-ceramic sheet for ionic and electronic conductivity measurements. Electronic conductivity was determined using a galvanostatic test on a Solartron 1287 potentiostat with 0.5 V applied for 20 h. While the second layout shown in Fig. 1b had approximately 4 μm of lithium metal evaporated using a 900 W MDC Vacuum Products Corporation power supply at 100 A current and a rate of 20 \AA s^{-1} onto both sides of several samples to allow for galvanostatic cycling tests of repeated deposition and stripping of lithium to determine the electrochemical stability of the material with Lithium metal. The cycles were carried out between 0.35 mA cm^{-2} and 0.175 mAh cm^{-2} for 200 h at 25 °C. The third layout of samples shown in Fig. 1c had ceramic powder tape-casted onto copper foil carrier foil for conductivity and galvanostatic lithium cycling tests. The copper foil was cleaned using acetic acid to remove the native copper oxide prior to coating the glass on the foil. These samples were then melt quenched using the same method as previously mentioned. Excess lithium metal was evaporated onto the top side of the sample to allow for galvanostatic cycling tests. Lithium metal was deposited in situ on the samples between the copper foil and glass to create a lithium symmetric half-cell. In situ deposition of lithium metal has been previously demonstrated by Neudecker et al. at Oak Ridge National Labs (ORNL).³¹ The initial lithium metal deposition was carried out at low rates of 50 $\mu\text{A cm}^{-2}$ to overcome any interfacial impedance at the boundary layer. AC impedance measurements were taken before (Fig. 1(c1)) and after (Fig. 1(c2)) plating the in situ contact to compare conductivity. The fourth and final layout shown in Fig. 1d had ceramic powder casted onto stainless steel foil in the same manner as mentioned above. The samples were used for cyclic voltammetry testing with a Solartron 1287 potentiostat at a rate of 5 mV s^{-1} from -0.05 to 6.5 V, and 100 $\mu\text{V s}^{-1}$ from $-200 \mu\text{V}$ to 6.5 V.

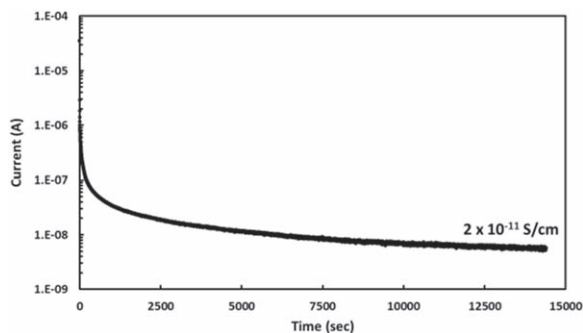


Figure 4. Chart showing current data from applying a 0.5 V constant voltage to a $\sim 17 \mu\text{m}$ thick and 1 cm^2 area glass electrolyte for 4 h and allowing the current to come to a steady state to determining electronic conductivity of glass electrolyte at room temperature.

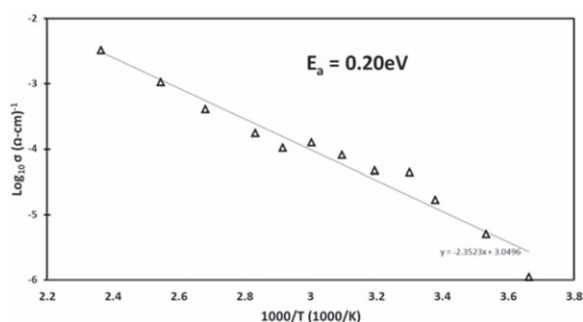


Figure 5. Arrhenius plot of glass electrolyte. showing $\sim 2 \times 10^{-5} \text{ s cm}^{-1}$ ionic conductivity at room temperature and an activation energy of 0.20 eV.

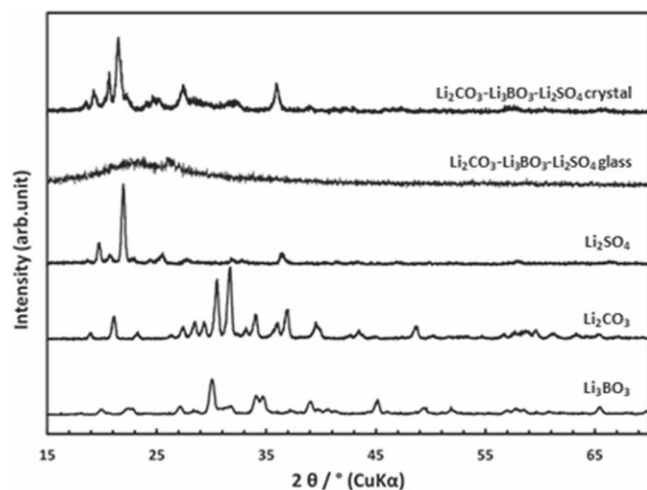


Figure 6. XRD patterns of patented $^{30} \text{Li}_2\text{CO}_3\text{-Li}_3\text{BO}_3\text{-Li}_2\text{SO}_4$ glass and crystal, along with precursor materials Li_2CO_3 , Li_3BO_3 , and Li_2SO_4 .

Results

SEM images of the cross sectional and surface of the melt quench glass are shown in Fig. 2. Fig. 2a shows a very smooth surface with little imperfections. This is further complemented in Fig. 2b shows a very dense and thin ($\sim 5 \mu\text{m}$) cross section without pinholes or defects. The nyquist plot of the electrolyte is shown in Fig. 3. The open square curve represents the impedance of the glass before in situ deposition of lithium to the glass-copper foil interface (layup shown in Fig. 1(c1)). This conductivity was determined to be $3 \times 10^{-6} \text{ s cm}^{-1}$. The open diamond curve represents the impedance after in situ deposition of lithium to the glass-copper foil interface (layup shown in Fig. 1(c2)). The impedance of the glass decreased

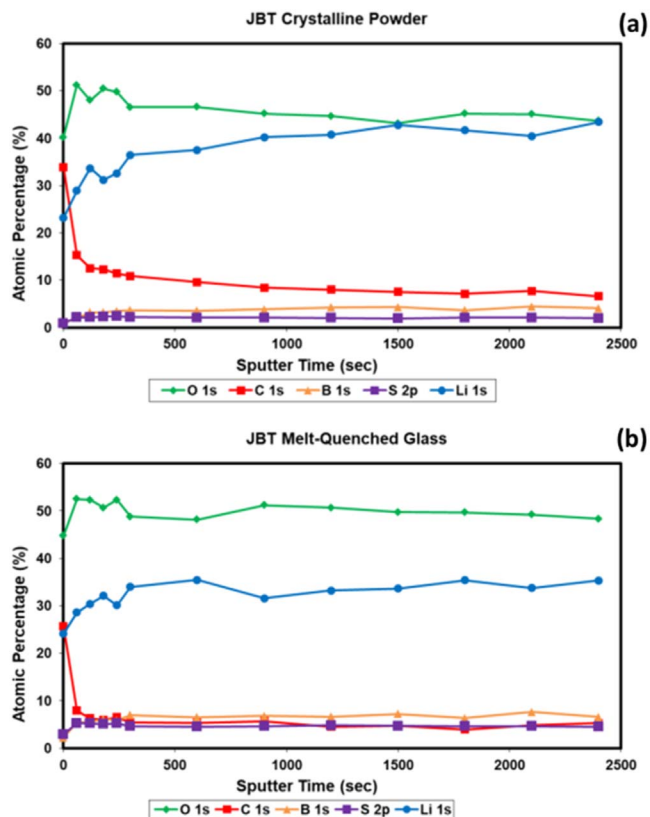


Figure 7. XPS of the patented 30 pre (a) and post (b) roll quenched material detailing chemical composition at the surface.

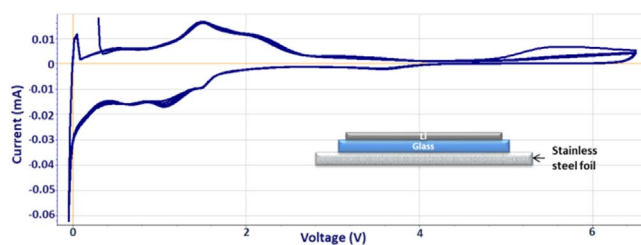


Figure 8. Cyclic voltammety of glass ceramic on stainless steel current collector substrate at room temperature tested by independent battery manufacturer at 5 mV s^{-1} from -0.05 V to 6.5 V for 3 cycles.

by almost an order of magnitude corresponding to a conductivity increase of approximately an order of magnitude to $2 \times 10^{-5} \text{ s cm}^{-1}$. Figure 4 shows the galvanostatic test for determining electronic conductivity of a $\sim 17 \mu\text{m}$ thick and 1 cm^2 area glass electrolyte using copper and gold ion-blocking contacts. The steady state current achieved in the test is $5.7 \times 10^{-9} \text{ A}$ after 4 h under 0.5 V bias and correlates to an electronic conductivity of $2 \times 10^{-11} \text{ s cm}^{-1}$. That is approximately 6 orders of magnitude separation from the ionic conductivity shown in Fig. 3b. The Arrhenius plot of the glass is shown in Fig. 5. The activation energy of the glass was calculated to be 0.2 eV from the Arrhenius equation. Figure 6 shows a comparison of the XRD patterns of the crystalline powder, melt-quench glass and precursors of the glass. The sharper peaks observed in the crystalline powder can be attributed to Li_2SO_4 and Li_2CO_3 . While the broad peaks indicates the material as semi-crystalline in nature. The melt quench glass shows the absence of any sharp diffraction peaks. Figure 7 shows a summary of the XPS results of the crystalline powder (a) and the melt quench glass (b). There are elevated levels of carbon in the powder and reduced level of lithium in the glass. Figure 8 was generated by an independent battery manufacturer and it

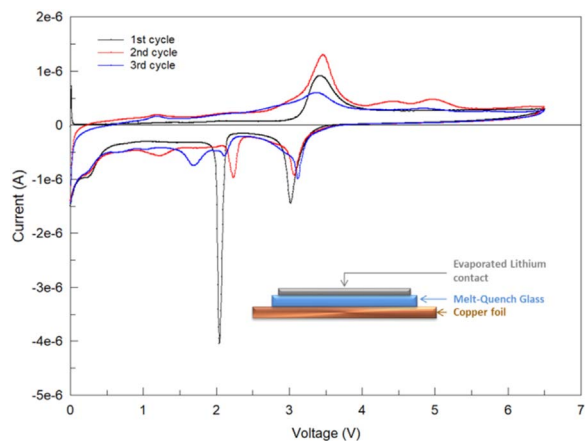


Figure 9. Cyclic voltammety of glass ceramic on copper current collector substrate at room temperature at $100 \mu\text{V s}^{-1}$ from $-200 \mu\text{V}$ to 6.5 V for 3 cycles.

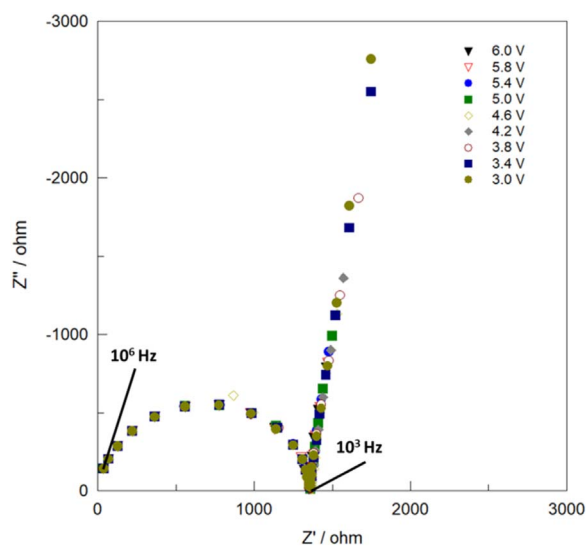


Figure 10. EIS of glass ceramic sample of $20 \mu\text{m}$ thickness and 1 cm^2 area at different voltages from 3 to 6 V in increments of 0.4 V generated during a CV test conducted at room temperature. There is no change in impedance. The slight changes seen are mostly related to low frequency area slop of Warburg.

shows the cyclic voltammety of the glass sample shown in Fig. 1d. An oxidation reaction is seen around 5.1 V but disappears after cycling up to 6.5 V. All other redox reactions are stable and reversible. A slower rate CV test was also conducted using the layout as illustrated in Fig. 1(c1). The curve is shown in Fig. 9. An anodic peak was seen at $\sim 3.4 \text{ V}$ while cathodic peaks were seen at $\sim 3.1 \text{ V}$ and $\sim 2 \text{ V}$ on the first cycle. On the second cycle the cathodic peak that seen at $\sim 2 \text{ V}$ seemed to have shifted to the right and was greatly reduced in amplitude. The series of Nyquist plots shown in Fig. 10 were generated at various voltages from 3 to 6 V in increments of 0.4 V during a CV scan of the glass ceramic on a copper current collector substrate. The absence of any significant changes in the Nyquist plot proves that the glass is stable with lithium metal. Figure 11 shows the galvanostatic cycling of a lithium/glass-ceramic electrolyte/in situ lithium/copper foil sample at a current density of 0.35 mA cm^{-2} and capacity density of $0.175 \text{ mAh cm}^{-2}$. A zoomed in view of cycles 24, 177 and 335 are shown in the inset. The overpotential initially increases to $\sim 50 \text{ mV}$ around hour 10 but gradually decreases to $\sim 15 \text{ mV}$ around hour 20 and relatively stays at this voltage until around hour 90 where the voltage slowly increases

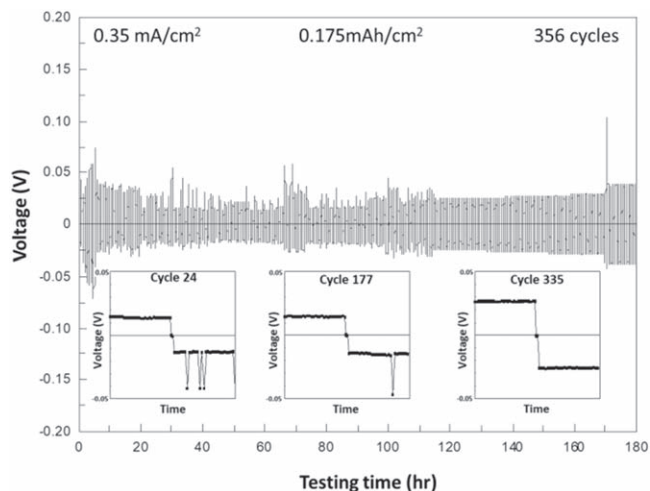


Figure 11. Galvanic cycling of Li/glass-ceramic electrolyte/Li symmetric cell at 0.35 mA cm^{-2} and $0.175 \text{ mAh cm}^{-2}$ at room temperature. Zoomed in view of cycles 24, 177 and 335 are shown in inset.

until hour 170 where it stabilizes. No voltage tails or arcs were seen on the zoomed in view as the sample cycled, but the slight increase in the overpotential during cycling was confirmed moving from $\sim 15 \text{ mV}$ on cycle 24 to $\sim 25 \text{ mV}$ on cycle 335.

Discussion

The ability to make the separator less than $10 \mu\text{m}$ as shown in Fig. 2b is important to reduce its footprint in the battery. A separator with a thin cross-section is necessary to reduce its contribution to the overall weight and volume of the battery in order to improve its energy density.²² A thinner separator also compensates for the slightly lower conductivity of this glass compared to liquid electrolytes or other higher conductive solid electrolytes such as LLZO or the sulfides which cannot be made as thin unless it is supported on a current collector substrate.^{14,19,24,25,28,32,33} The ability to make the glass as thin as $6 \mu\text{m}$ or less along with an ionic conductivity of $1 \times 10^{-5} \text{ s cm}^{-1}$, gives an ASR of less than $30 \Omega \cdot \text{cm}^2$ which is necessary to achieve high current densities. Achieving thin electrolyte layer is enabled by our unique melt quench process coupled with the use of a current collector substrate.

The change in ionic conductivity seen after in situ deposition of lithium to the copper-glass interface suggests that there may be a resistive interfacial layer between the glass and the copper foil that must be overcome to get the true impedance of the glass. To confirm the presence of such a layer, the ionic conductivity of the free standing glass sheets with lithium contacts as shown in Fig. 1b were measured and compared to the conductivity of lithium deposited on glass on copper foil before in situ lithium deposition (Fig. 1c(1) and Fig. 1c(2) after in situ lithium deposition. The conductivity of the sample in Fig. 1b was similar to the conductivity of the sample in Fig. 1c(2) which was approximately an order of magnitude higher than the conductivity of the sample in Fig. 1c(1) (as shown in nyquist plots in figure), confirming the presence of a resistive layer between the copper and glass interface. This layer could be that there is a parasitic reaction between the glass and the copper foil during melt quenching of the glass. More research is needed to identify what the layer is, how it was formed and how it impacts the operation of the electrolyte.

The electronic conductivity was determined by applying a constant voltage to the electrolyte, the current will initially decrease rapidly and then come to a steady state. This steady state current is determined to be the electronic leakage of the glass. In this study the conductivity was measured using ion-blocking electrodes (gold and copper) and is not the same as the Wagner-Hebb method (using an

ion blocking and lithium metal electrode). It instead provides an upper limit of the electronic conductivity.²⁵ Han et al. showed that LiPON has been proven to prevent dendrites up to a critical current density greater than 10 mA cm^{-2} because of its low electronic conductivity (10^{-15} – $10^{-12} \text{ s cm}^{-1}$) while LLZO will start shorting at current density of 1 mA cm^{-2} because of its higher electronic conductivity (10^{-8} – $10^{-7} \text{ s cm}^{-1}$).²⁵ The Li_2CO_3 – Li_3BO_3 – Li_2SO_4 glass-ceramic has an electronic conductivity of $10^{-11} \text{ s cm}^{-1}$ that is 3 orders of magnitude lower than LLZO suggesting that its critical current density would be greater than that of LLZO and closer to that of LiPON. The exact critical current density will be determined and published in a later article.

A low activation energy is necessary for a solid electrolyte to achieve stable performance across wide temperature ranges³⁴ and also to improve lithium diffusion through the electrolyte.³⁵ The activation energy for a few well-studied electrolytes such as LLZO,³⁶ nanoporous β - Li_2S - P_2S_5 ,³⁷ $\text{Li}_{10}\text{GeP}_2\text{S}_{12}$ ³⁸ and LIPON³⁹ are 0.26 eV, 0.356 eV, 0.249 eV and 0.55 eV respectively. As can be seen the activation energy of 0.2 eV for the Li_2CO_3 – Li_3BO_3 – Li_2SO_4 glass-ceramic is among the lowest activation energy reported in literature for a solid electrolyte.

The absence of peaks in the XRD pattern of the Li_2CO_3 – Li_3BO_3 – Li_2SO_4 glass is evidence that amorphous samples were obtained by the twin roll quench method.

The elevated levels of carbon in the crystalline powder can be attributed to the fact that sheets of the crystalline material were made in air and were further planetary ball milled in solvent to achieve powder. During these processes the powder could react with moisture and carbon dioxide in the air or any residual moisture in the solvent during milling. While the melt quench material was made in an inert Ar filled environment free from contamination from moisture and carbon dioxide, hence the reason for the lower presence of carbon. It is expected for the crystalline powder to have a greater quantity of contaminants because of the dramatic increase in surface area going from a micron sized crystalline powder compared to the centimeter sized melt-quench glass sheets. The loss in lithium in the melt quenched glass is due to lithium volatilization causing evaporation at elevated temperatures^{33,40} during the melting of the glass

From the slower rate CV chart in Fig. 9, there is a reversible reaction happening at anodic peak at $\sim 3.4 \text{ V}$ and cathode peak at $\sim 3.1 \text{ V}$ that is attributed to the oxidation and reduction of copper in the presence of the glass-ceramic. The cathodic peak at ~ 1.5 – 2.5 V is attributed to the reduction of the native copper oxide on the copper foil.⁴¹ The cathodic peaks at ~ 1 and between 4 – 5 V are not identified. Future work will be geared towards conducting a CV test on a free standing glass sample with lithium contacts as shown in Fig. 1b to separate the effects of the carrier foil from the scan.

The lack of an increase in impedance in the series of EIS in Fig. 10 is evidence that the glass is stable with lithium metal in the measured voltage range. The changes seen are mostly related to low frequency area slope of the Warburg. The impedance of the glass is stable while cycling up to 6 V .

Relatively stable overpotential and flat voltage plateaus during galvanic cycling of the lithium/glass electrolyte/in situ lithium/copper foil sample is an indication that it is stable with lithium metal anode. The slight increase in overpotential during the galvanostatic cycling test up to cycle 170 followed by an immediate stabilization may be due to the slow formation of a passivating interfacial layer between the glass and lithium metal as mentioned by Nagao et al.⁵²

Conclusions

A patented proprietary ternary oxide glass-ceramic electrolyte Li_2CO_3 – Li_3BO_3 – Li_2SO_4 was synthesized using melt quenching techniques that can allow application to solid-state cathodes or metal substrates as a thin film. The glass-ceramic system shows a pre-quench conductivity of 1.0×10^{-6} – $3.0 \times 10^{-6} \text{ s cm}^{-1}$ and a

conductivity of $\sim 1.0 \times 10^{-5} \text{ s cm}^{-1}$ when quenched to a semi-crystalline state. The glass-ceramic was shown to be stable with Lithium metal during cycling with no dendrite formations leading to shorts. Applying the glass at a thickness of $\sim 6 \mu\text{m}$ results in an ASR of less than $30 \Omega\text{-cm}^2$, overcoming conductivity limitation and minimizing its volumetric and gravimetric contribution to the total cell. These properties make this glass-ceramic system a viable electrolyte for SSB systems and possible hybrid solid-liquid systems. Future work will continue to explore the material behavior in full cell designs.

Acknowledgments

We would like to thank Johnson Battery Technologies Inc. for providing funding for this research.

Appendix

ORCID

Adrian Grant  <https://orcid.org/0000-0003-0307-2838>

Devon Lyman  <https://orcid.org/0000-0003-1367-0583>

References

1. Y. Lu, L. Yu, and X. W. (David) Lou, *Chem*, **4**, 972 (2018).
2. X. Wu, K. Song, X. Zhang, N. Hu, L. Li, W. Li, L. Zhang, and H. Zhang, *Front. Energy Res.*, **7**, 65 (2019).
3. J. T. Warner, "Chapter 3—Lithium-ion battery operation." *Lithium-Ion Battery Chemistries* (Elsevier, Amsterdam) p. 43 (2019).
4. D. Ouyang, M. Chen, Q. Huang, J. Weng, Z. Wang, and J. Wang, *Applied Sciences*, **9**, 2483 (2019).
5. L. Kong, C. Li, J. Jiang, and M. Pecht, *Energies*, **11**, 2191 (2018).
6. W. Xu, J. Wang, F. Ding, X. Chen, E. Nasybulin, Y. Zhang, and J.-G. Zhang, *Energy Environ. Sci.*, **7**, 513 (2014).
7. X. He, X. Liu, Q. Han, P. Zhang, X. Song, and Y. Zhao, *Angew. Chem. Int. Ed.*, **59**, 6397 (2020).
8. J. Kalthoff, G. G. Eshetu, D. Bresser, and S. Passerini, *Chem. Sus. Chem.*, **8**, 2154 (2015).
9. K. Chung, W.-S. Kim, and Y.-K. Choi, *J. Electroanal. Chem.*, **566**, 263 (2004).
10. N. J. Dudney, *J. Power Sources*, **89**, 176 (2000).
11. Y. Liu et al., *ACS Appl. Mater. Interfaces*, **10**, 31240 (2018).
12. M. Ogawa, R. Kanda, K. Yoshida, T. Uemura, and K. Harada, *J. Power Sources*, **205**, 487 (2012).
13. R. Pathak et al., *Nat. Commun.*, **11**, 93 (2020).
14. H. Duan, Y.-X. Yin, Y. Shi, P.-F. Wang, X.-D. Zhang, C.-P. Yang, J.-L. Shi, R. Wen, Y.-G. Guo, and L.-J. Wan, *J. Am. Chem. Soc.*, **140**, 82 (2018).
15. A. Manthiram, X. Yu, and S. Wang, *Nat Rev Mater*, **2**, 16103 (2017).
16. Z. Shen, W. Zhang, G. Zhu, Y. Huang, Q. Feng, and Y. Lu, *Small Methods*, **4**, 1900592 (2020).
17. P. Hartmann, T. Leichtweiss, M. R. Busche, M. Schneider, M. Reich, J. Sann, P. Adelhelm, and J. Janek, *J. Phys. Chem. C*, **117**, 21064 (2013).
18. S. Wenzel, S. Randau, T. Leichtweiß, D. A. Weber, J. Sann, W. G. Zeier, and J. Janek, *Chem. Mater.*, **28**, 2400 (2016).
19. P. Barai, A. T. Ngo, B. Narayanan, K. Higa, L. A. Curtiss, and V. Srinivasan, *J. Electrochem. Soc.*, **167**, 100537 (2020).
20. H.-K. Tian, B. Xu, and Y. Qi, *J. Power Sources*, **392**, 79 (2018).
21. S. Liu, N. Imanishi, T. Zhang, A. Hirano, Y. Takeda, O. Yamamoto, and J. Yang, *J. Power Sources*, **195**, 6847 (2010).
22. J. Kasemchainan and P. G. Bruce, *Johnson Matthey Technology Review*, **62**, 177 (2018).
23. X. Yu, J. B. Bates, G. E. Jellison Jr, and F. X. Hart, *J. Electrochem. Soc.*, **144**, 524 (1997).
24. C. Wang, G. Bai, Y. Yang, X. Liu, and H. Shao, *Nano Res.*, **12**, 217 (2019).
25. F. Han, A. S. Westover, J. Yue, X. Fan, F. Wang, M. Chi, D. N. Leonard, N. J. Dudney, H. Wang, and C. Wang, *Nat. Energy*, **4**, 187 (2019).
26. A. Patil, V. Patil, D. Wook Shin, J.-W. Choi, D.-S. Paik, and S.-J. Yoon, *Mater. Res. Bull.*, **43**, 1913 (2008).
27. X. Zeng, M. Li, D. Abd El-Hady, W. Alshitari, A. S. Al-Bogami, J. Lu, and K. Amine, *Adv. Energy Mater.*, **9**, 1900161 (2019).
28. C. Wang et al., *Nano Energy*, **48**, 35 (2018).
29. N. M. Asl, J. Keith, C. Lim, L. Zhu, and Y. Kim, *Electrochim. Acta*, **79**, 8 (2012).
30. L. Allie, A. Grant, D. Lyman, L. Johnson, and D. Johnson, "Solid-state batteries, separators, electrodes, and methods of fabrication." US10566611B2 (2020), <https://patents.google.com/patent/US10566611B2/en?qoq=10566611>.
31. B. J. Neudecker, N. J. Dudney, and J. B. Bates, *J. Electrochem. Soc.*, **147**, 517 (2000).
32. K. Nagao, M. Nose, A. Kato, A. Sakuda, A. Hayashi, and M. Tatsumisago, *Solid State Ionics*, **308**, 68 (2017).

33. S. Kumar, S. Ramnathan, and N. Krishnamurthy, *PAC*, **5**, 13 (2011).
34. G. Sahu, E. Rangasamy, J. Li, Y. Chen, K. An, N. Dudney, and C. Liang, *J. Mater. Chem. A*, **2**, 10396 (2014).
35. R. Gopalakrishnan, O. Capron, J.-M. Timmermans, X. Zhu, N. Omar, A. Hubin, and J. V. Mierlo, *Meet. Abstr.*, **MA2017-01**, 37 (2017), <https://iopscience.iop.org/article/10.1149/MA2017-01/1/37>.
36. E. Rangasamy, J. Wolfensine, and J. Sakamoto, *Solid State Ionics*, **206**, 28 (2012).
37. Z. Liu, W. Fu, E. A. Payzant, X. Yu, Z. Wu, N. J. Dudney, J. Kiggans, K. Hong, A. J. Rondinone, and C. Liang, *J. Am. Chem. Soc.*, **135**, 975 (2013).
38. N. Kamaya et al., *Nature Mater*, **10**, 682 (2011).
39. L. Le Van-Jodin, F. Ducroquet, F. Sabary, and I. Chevalier, *Solid State Ionics*, **253**, 151 (2013).
40. W. Xue, Y. Yang, Q. Yang, Y. Liu, L. Wang, C. Chen, and R. Cheng, *RSC Adv.*, **8**, 13083 (2018).
41. S.-T. Myung, Y. Hitoshi, and Y.-K. Sun, *J. Mater. Chem.*, **21**, 9891 (2011).